Inorganic Chemistry Communications 159 (2024) 111806

Contents lists available at ScienceDirect

Inorganic Chemistry Communications

journal homepage: www.elsevier.com/locate/inoche

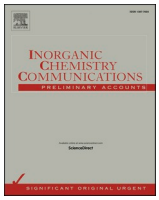

Short communication

Exploring a new creatininium crystalline salt with succinic acid organic counterion: Structural establishment, spectroscopic analysis and theoretical simulation

Wahiba Falek [a], Radhwane Takouachet [a], Rim Benali-Cherif [a,*], Sonia Baaziz [a], Nourredine Benali-Cherif [b,c]

[a] Laboratoire des Structures, Propriétés et Interactions Interatomiques (LASPI²A), Université Abbes Laghrour-Khenchela, 40000 Khenchela, Algeria
[b] Académie Algérienne des Sciences et de la Technologie (AAST) Algiers, Algeria
[c] University of JIJEL, BP 98 Ouled Aissa, Jijel 18000, Algeria

A B S T R A C T

This study elucidates the structural, vibrational, and electronic properties of a novel proton-transfer system derived from creatinine and succinic acid named bis (creatininium) succinate (I). Fourier maps and geometric evaluations confirm protonation at the imine sites. Spectroscopic analyses, involving both IR and Raman techniques, were conducted, highlighting the vibrational characteristics of key functional groups. The theoretical predictions of structural parameters and vibrational frequencies align well with experimental findings. Frontier Molecular Orbital analysis emphasized the distinct localization of HOMO and LUMO, hinting at potential intramolecular charge transfers. Molecular Electrostatic Potential maps provided a visual testament to regions of electron density and scarcity, offering predictive insights into reactivity. Hirshfeld surface analysis and fingerprint plots further illuminated the intermolecular interactions within the crystal structure, underscoring the significance of hydrogen bonding in lattice cohesion. The results present a comprehensive understanding of the compound's behaviour, potentially impacting fields demanding molecular stability and specificity.

1. Introduction

Organic salts, formed by the proton transfer between organic acids and bases, have garnered substantial attention in recent years due to their diverse structural motifs, unique physicochemical properties, and potential applications in various fields such as nonlinear optics, pharmaceuticals, and organic electronics [1–4]. A promising approach in the discovery of new materials with tailored properties involves pairing known organic cations and anions in innovative ways, capitalizing on their complementary structural and interactive features [5–7].

One such potential organic cation of interest is creatinine. Creatinine, a naturally occurring nitrogenous compound, is a byproduct of muscle metabolism and is derived from the degradation of creatine phosphate [8]. Its presence in the bloodstream and its rate of excretion in urine are indicators of kidney function, making it a critical biomarker in clinical settings [9]. On the other hand, succinic acid stands out as a potential anion counterpart. Historically sourced from amber, succinic acid is a dicarboxylic acid involved in the citric acid cycle, making it pivotal for energy production in organisms [10]. Succinic acid's value as a bio-based building block chemical has been recognized, especially in the production of industrial products, from bioplastics to solvents and food additives [11].

The decision to pair these two molecules isn't arbitrary. Intermolecular interactions, particularly hydrogen bonding, underpin the assembly of molecules in specific orientations and arrangements in crystalline structures [12]. The inherent hydrogen bonding capability of creatinine, combined with the dual acid functionalities in succinic acid, promises a robust interaction. These interactions, which also include van der Waals and dipole–dipole interactions, influence numerous properties from solubility and melting point to mechanical and optical characteristics [13,14]. The properties discussed earlier are deeply influenced by structural organizations and intermolecular interactions. Grasping how these interactions affect the structural attributes is vital for designing materials tailored with specific functionalities [15].

Indeed, following an in-depth analysis on the Cambridge Structural Database (CSD, ConQuest Version 2023.2.0) [16] for crystal structures containing creatininium cations results in 34 hits, and for succinate anions results in 595 hits. These findings show how common and important these molecular structures are in crystallography. However, it's evident that while the applications of established organic salts are of

* Corresponding author.
E-mail address: benalicherif.rim@univ-khenchela.dz (R. Benali-Cherif).

https://doi.org/10.1016/j.inoche.2023.111806
Received 12 September 2023; Received in revised form 16 November 2023; Accepted 23 November 2023
Available online 28 November 2023

immense importance, venturing into the uncharted territories of undiscovered ones presents a broader spectrum of opportunities. Every new organic salt synthesized and characterized offers chemists a fresh palette of possibilities, ripe with both challenges and rewards [17].

To further elucidate the nature of intermolecular interactions, Hirshfeld surface analysis was employed. This powerful technique provides visual and quantitative insight into the close contacts within the crystal structure, emphasizing the significance of individual interactions and their contribution to the overall stability and arrangement of molecules within the lattice.

The study of organic salts, particularly those formed from biologically relevant molecules like creatinine and succinic acid, has garnered increasing attention in recent years [18]. Research in this area has largely focused on understanding the physicochemical properties and potential applications of these compounds in various domains, including pharmaceuticals [19], materials science, and biochemistry [20,21]. Notably, previous studies have explored the individual characteristics of creatinine and succinic acid in various contexts [22]. However, the exploration of their combined potential in forming novel organic salts, which could offer unique properties, remains relatively untapped.

Building upon this foundation, our research aims to explore the synthesis and characterization of bis(creatininium) succinate, delving into its structural, vibrational, and electronic properties. This approach aligns with recent advancements in the field where the focus is shifting towards hybrid organic salts that combine different molecular entities to achieve specific functional attributes [23,24]. Our study contributes to this emerging area of research, offering new insights into the potential synergistic effects and applications of these combined molecular systems.

Guided by these insights, in this study, we report the synthesis and comprehensive characterization of a novel organic salt, Bis(creatininium) succinate (Scheme 1). Through the X-ray diffraction technique, we provide insights into its crystallographic parameters and the intricate network of intermolecular interactions. Complementary vibrational spectroscopy methods, including Infrared (IR) and Raman Spectroscopy, offer additional depth to its molecular and lattice dynamics. Augmenting our experimental work, computational calculations were undertaken to understand these interactions at a theoretical level, harmonizing our experimental observations with theoretical predictions. This integrated approach not only affirms the formation of the synthesized salt but also delves into the reasons behind its stability and unique arrangement in the crystalline state.

In this study, the application of density functional theory (DFT) is pivotal in complementing our experimental findings and providing a deeper theoretical understanding of bis(creatininium) succinate. DFT has enabled us to precisely predict the structural and electronic properties of the compound, thus offering invaluable insights that bridge the gap between theoretical predictions and experimental observations. Such comprehensive theoretical analysis not only corroborates our experimental results but also enhances our understanding of the compound's potential reactivity and applications. The integration of DFT thus plays a key role in our study, contributing significantly to the advancement of our knowledge in the field of organic salt chemistry.

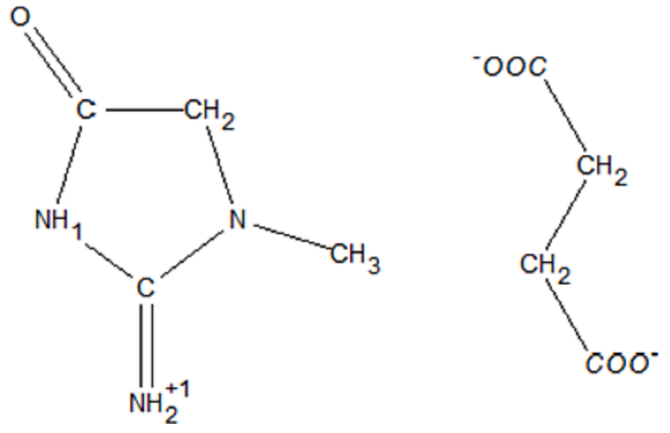

Scheme 1. Chemical diagram of Bis (creatininium) succinate.

Building on the understanding that previous research into the individual behavior of succinate or creatininium compounds is extensive, yet lacks a combined molecular structure, electronic properties, and interaction dynamics analysis within a single system, our study to bridge this knowledge gap. It does so by presenting an exhaustive multi-technique analysis that not only includes X-ray crystallography and vibrational spectroscopy but also extends to frontier molecular orbital (FMO) analysis, molecular electrostatic potential (MEP), and Hirshfeld surface analysis. This integrative approach equips our study with a unique position in the current literature, providing an unprecedented view of the system's stability, electronic behavior, and interaction dynamics.

The significance of our work lies in its potential to advance the fields of molecular engineering and materials science, offering novel perspectives for designing materials with tailored properties. Looking forward, our findings lay a solid foundation for future explorations into the applications of such organic salts in various industrial and pharmaceutical contexts, potentially leading to the development of innovative materials and drugs.

2. Experimental

2.1. Synthesis and crystallization

All chemicals (reagents and solvents) were used as purchased from Sigma–Aldrich without further purification. Single crystals of $C_4H_4O_4{\cdot}2(C_4H_8N_3O)$ were grown by the slow evaporation solution growth technique at room temperature. In a stoichiometric ratio, creatinine (0.5 g, 0.0044 mol) dissolved in water (25 ml) was slowly added under stirring to succinic (0.5 g, 0.0042 mol) and mixed using a magnetic stirrer to ensure homogeneous concentration in the entire volume of the solution. Colourless transparent block crystals started to form after a few weeks.

2.2. Single crystal X-ray diffraction and structure refinement details

The single crystal diffraction measurements of (I) were performed on an Oxford Gemini diffractometer with a graphite monochromatized MoK α radiation, $\lambda = 0.71073$ Å. Crystal data, data collection and structure refinement details of (I) are summarized in Table 1. The structure has been solved by direct methods using the program SIR2018 [25] and was refined against F^2 by weighted full-matrix least squares methods including all reflections with SHELXL-2018 program [26]. All calculations were carried out using WingX software package [27]. Structural representations were drawn using MERCURY [28]. Analytical absorption corrections were performed [29]. All non-H atoms were refined anisotropically. All hydrogen atoms have been placed by calculations.Table 2..

2.3. Computational details

The X-ray crystal structure was employed to determine the energies and electronic properties. Computations were performed under periodic boundary conditions (PBC) for (I) at the DFT level. We utilized the hybrid B3LYP functional [30] and the 6–31 G (d, p) basis sets [31]. Previous studies have confirmed that the B3LYP functional offers structural properties that align closely with experimental findings [32,33]. All computations were executed using Gaussian 09 [34]. For visual interpretation and assessment of the computed data, we employed Gaussview [35] and GaussSum [36] software tools.

Table 1
Main crystallographic data and structure refinement details for (I).

Crystal data	
Empirical Formula	$C_4H_4O_4{\cdot}2(C_4H_8N_3O)$
Molecular weight (g/mol)	172.15
Diffractometer,	Oxford Diffraction Gemini
Radiation type	Mo Kα ($\lambda = 0.71073$ Å)
***T* (K)**	293
Calculated density (Mg/m^3)	1.44
Crystal system	Orthorhombic
Space group	*Fdd2*
***a* (Å)**	40.167 (3)
***b* (Å)**	14.2908 (11)
***c* (Å)**	5.5320 (5)
***V* (Å^3)**	3175.5 (4)
Z	8
***μ* (mm^{-1})**	0.12
Crystal size (mm)	0.58 × 0.30 × 0.22
T_{min}, T_{max}	0.96, 0.97
No. of measured, independent and observed [$I > 2\sigma(I)$] reflections	2911, 1524, 1306
R(int)[a] **Refinement**	0.022
$R[F^2 > 2\sigma(F^2)]$ [b], $wR(F^2)$ [c], S [d]	0.040, 0.100, 1.10
No. of parameters	110
$\Delta\rho_{max}$, $\Delta\rho_{min}$ (e Å^{-3})	0.17, −0.17

[a] $R(\text{int}) = \Sigma(F_o^2 - <F_o^2>)] / \Sigma(F_o^2)$.
[b] $R_1 = \Sigma||F_o|-|F_c|| / \Sigma|F_o|$.
[c] $wR_2 = \{[\Sigma w(F_o^2-F_c^2)^2] / [\Sigma w(F_o^2)^2]\}^{1/2}$.
[d] Goodness-of-fit $S = [\Sigma w(F_o^2 - F_c^2)^2/(n-p)]^{1/2}$, where n is the number of reflections and p the number of parameters.

Table 2
Hydrogen-bond geometry (Å, °).

D—H···A	D—H	H···A	D···A	D—H···A
N1—H1···O2	0.86	1.81	2.665 (3)	171
C4—H4A···O2^{ii}	0.97	2.61	3.532 (3)	158
N2—H2A···O1^{iii}	0.86	1.95	2.783 (3)	163
N2—H2B···O1	0.86	1.91	2.754 (3)	165
C3—H3B···O5^{ii}	0.96	2.43	3.346 (4)	159
C3—H3C···O2^{iv}	0.96	2.58	3.491 (4)	160

Symmetry codes: (ii) − x+¼, y+¼, z−¾; (iii) − x, −y+½, z−½; (iv) x, y+½, z−½.

2.4. Hirshfeld surface (HS) calculations

Hirshfeld surfaces (HS) [37] were generated using electron distributions computed as the sum of spherical electron densities associated with atoms [38]. When a specific crystal structure and a set of spherical atomic electron densities are given, the resulting HS is distinct and unique [39]. This approach has gained growing popularity for analyzing all interactions present within the structure. Utilizing the CrystalExplorer software [40], we calculated both three-dimensional HS and two-dimensional fingerprint plots for (I), with visualization based on the normalized contact distance (d_{norm}).

2.5. Infra-red and Raman spectroscopy

The FT-IR spectrum of (I) was obtained using the KBr pellet method from 4000 to 500 cm^{-1}, utilizing a Bruker Optics IFS66v/s FT-IR spectrometer with a 2 cm^{-1} resolution. The Raman spectrum was recorded in powder form using a Bruker Senterra Dispersive Raman microscope spectrometer, employing a 532 nm excitation 3B diode laser having a 2 cm^{-1} resolution over a spectral range of 3500 to 0 cm^{-1}. The IR and Raman spectra presented in this study were plotted using Origin software, version 6 [41].

3. Results and discussion

3.1. Structural description

The title compound (I) is a new proton-transfer system obtained from creatinine and succinic acid. The asymmetric unit consists of one creatininium cation ($C_4H_8N_3O^+$) and half a succinate dianion [0.5 ($C_4H_4O_4^{2-}$)](Fig. 1). The crystal structure of (I) shows that protons from two of the carboxyl groups are transferred to the endocyclic N atoms of two creatinine molecules. Firstly, this evidence is confirmed by observing the proton's position in difference density Fourier maps. The geometric environment of the imine (angles and distances) confirms their protonations on N1. And secondly by analyzing the lengths of the C—O bonds within the carboxyl group present in the acid moiety. These values are 1.249(16) and 1.251(17) Å for C6 ⎓ O1 and C6 ⎓ O2 respectively, indicating an ionized state of the carboxyl groups. The bond lengths observed fall between the typical lengths of single and double bonds. This indicates that the negative charge on the oxygen atom of the carboxylate is delocalized. This difference in the C—O bond lengths is connected with the hydrogen-bonding pattern, which uses both O atoms, namely the O1 atom makes two intermolecular N − H ··· O hydrogen bonds, while the O2 atom makes only one. The succinate anion is located across an inversion centre. the inversion center is at the midpoint of the C7—C7 simple bond. Moreover, in the succinate counterion, the carboxylate group is twisted with respect to the central C–CH_2–CH_2–C group with a dihedral angle of 64.6(3)°.

Cations are linked to succinate anions forming ion pairs through two hydrogen bonds; one via the imino group N1 atom, thus forming strong interactions (2.665(3) Å), and another via the amino N2 atoms (2.754 (3) Å), these two hydrogen bonds produce $R_2^2(8)$ ring motifs. This type of ring motif was observed in some salt creatininium-based [42,43].

The second amino hydrogen of the creatininium cation is connected to the carboxylate O1 atom of another succinate anion via N2—H2A ··· O1 hydrogen bond. On the other hand, the creatininium cation forms three hydrogen bonds of the C–H ··· O type. While these specific interactions might not exhibit the strength commonly associated with more conventional hydrogen bonds, such as those involving nitrogen or oxygen directly bonded to hydrogen, their contribution to the overall structure is undeniable. Despite their relatively weaker nature, the C–H ··· O interactions significantly bolster the cohesion of the crystal packing. The combination of these strong and moderate interactions led to the formation of $R_2^2(8)$, $R_2^2(14)$, $R_4^4(10)$, $R_4^3(13)$, $R_5^5(24)$ and $R_3^2(10)$ graph set motifs in the crystal structure (Fig. 2).

In the depicted molecular arrangement (Fig. 3), two creatininium molecules are interacting through electrostatic contacts. The O5 oxygen atom from one creatininium molecule uses its lone pair of electrons to engage in a dipole–dipole interaction with carbon atoms from the structure of the adjacent creatininium molecule. This interaction arises due to the electron-rich nature of the oxygen atom and the electron-deficient regions present on the carbons of the other molecule. Such interactions are important in molecular recognition and can influence the arrangement and stability of molecular assemblies.

This type of lone pair (O) to carbons (C) interaction is relatively rare, with the current instance representing only the second such observation among creatininium-based compounds present within the CSD [16]. The first identification of these contacts was recorded in the structure of Creatininium dihydrogen phosphite (REFCODE: XAXRIA) [44]. The recurrence of this specific interaction in such molecules underlines its potential significance in influencing the physicochemical properties of the resulting crystal lattice.".

The analysis of the interaction map in this investigation was conducted utilizing the MERCURY software [28] for structural visualization. As evident in Fig. 4, distinct interaction hotspots are delineated by the pronounced, opaque red and blue areas. In contrast, the more translucent red and blue zones represent less defined interaction

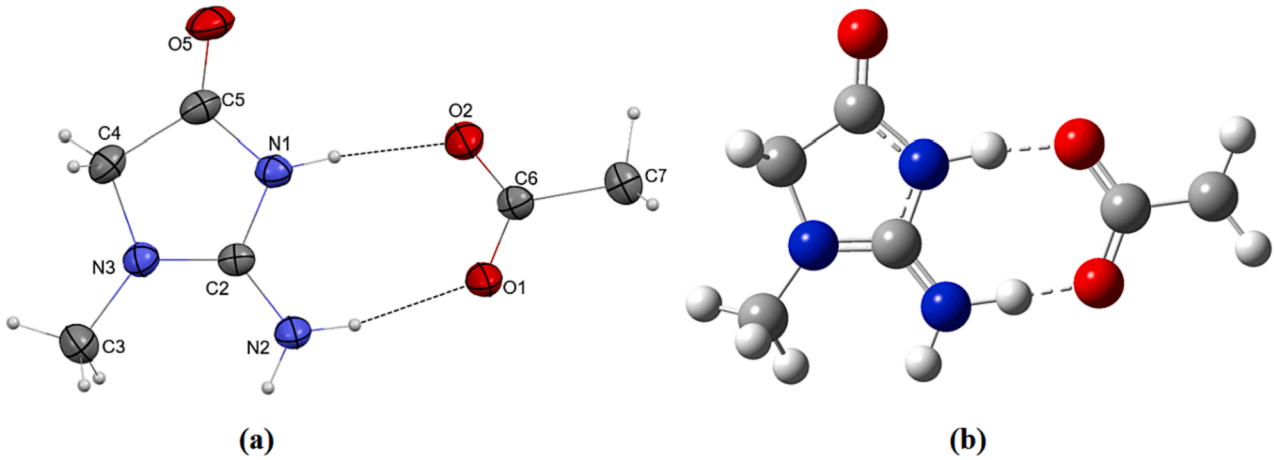

Fig. 1. (**a**) View of the asymmetric unit of (I) showing the immediate hydrogen-bonded between creatininium and succinate acid. Displacement ellipsoids are drawn at the 50% probability level and H atoms are shown as small grey spheres of arbitrary radius. (**b**) Optimized molecular structure of (I).

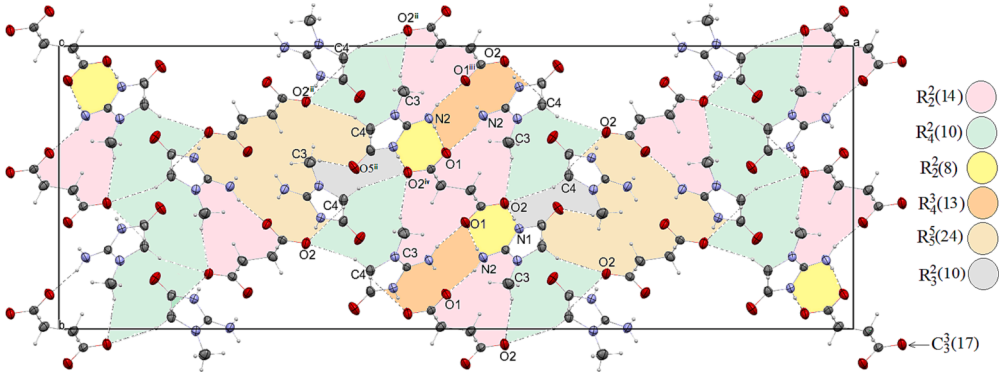

Fig. 2. Part of the packing diagram of (I) along the *c*-axis, showing the formation of $R_2^2(8)$, $R_2^2(14)$, $R_4^2(10)$, $R_4^3(13)$, $R_5^5(24)$ and $R_3^2(10)$ ring motifs and $C_3^3(17)$ infinite chain. Dashed lines indicate N–H ··· O and C–H ··· O hydrogen bonding interactions.

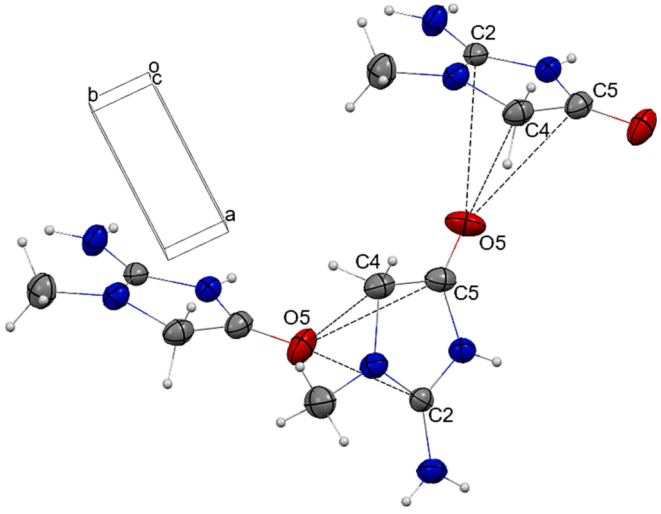

Fig. 3. $O_{lone\ pair}$ ··· Carbon electrostatic interactions between creatininium cations.

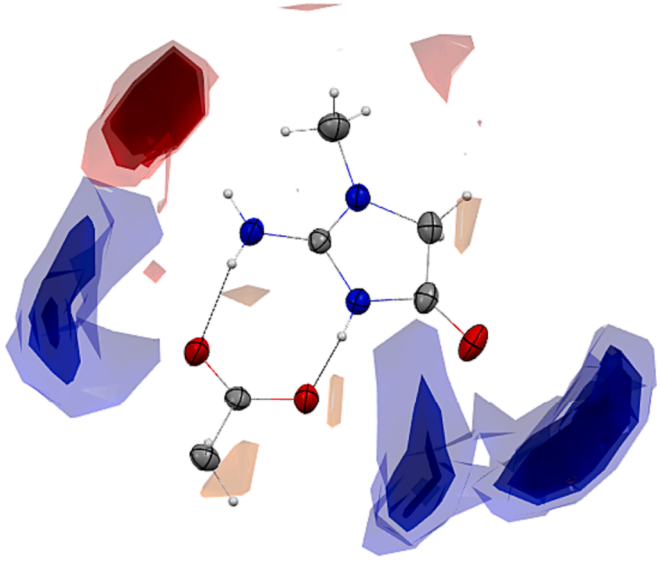

Fig. 4. Interaction maps shown around the asymmetric unit of (I).

regions. These contoured maps highlight regions of high interaction density. Blue hotspots, corresponding to the donor probe, suggest a predilection for interactions with the nitrogen acceptors present in the creatininium. Conversely, red hotspots, associated with the acceptor probe maps, signal the existence of the oxygen acceptor and certain weak $O_{lone\ pair}$–C interactions.

3.2. Spectroscopic analysis of vibrational modes

In the realm of molecular spectroscopy, the vibrational characteristics of functional groups play a pivotal role in understanding molecular structures and interactions. Both Infrared (IR) and Raman spectroscopy are quintessential techniques that provide insights into these vibrational modes. This study delves into the vibrational spectra of specific functional groups, comparing theoretical predictions with experimental observations from both IR and Raman spectra (Fig. 5). The C = O stretch in ketones and carboxylic acids is a defining feature of IR and Raman spectra, usually between 1870 and 1540 cm^{-1}. The simulated C = O stretch for (I) was at 1782 cm^{-1}, while the FTIR and Raman spectra showed it at 1714 and 1749 cm^{-1}, respectively.

This red shift in the experimental spectra, as compared to the theoretical predictions, is indicative of the influence of hydrogen bonding on the C = O group [45,46]. The hydrogen bonding interactions lead to a lengthening and weakening of the C = O bond, resulting in a lower vibrational frequency, a phenomenon critical for understanding the molecular interaction dynamics within bis(creatininium) succinate. The hydrogen bonding essentially stabilizes the C = O group in a lower energy state, thus shifting its vibrational frequency towards the red end of the spectrum.The pronounced intensity confirms intramolecular charge transfer within the molecule, amplifying the NLO activity [47].

NH_2 asymmetric and symmetric stretches are commonly found in the 3500–3333 cm^{-1} and 3330–3250 cm^{-1} ranges, respectively in FTIR and RAMAN spectra. The simulated NH_2 asymmetric stretch was detected at 3353 cm^{-1}. In the FTIR, the NH_2 symmetric stretch was observed at 3136 cm^{-1}, with corresponding simulated vibrations at 3199 and 3163 cm^{-1}. The NH_2 absorption's blue shift is attributed to the N–H ··· O hydrogen bond formation. The NH_2 scissoring motion is typically between 1700 and 1600 cm^{-1}, with the simulated spectrum showing peaks at 1730 and 1676 cm^{-1}. The hydrogen bonding here causes a slight increase in the bond strength of the NH_2 group, resulting in a higher vibrational frequency, which is observed as a blue shift.

The aromatic methyl group's asymmetric stretch typically manifests between 3000 and 2955 cm^{-1}. In the simulated spectrum, the CH_3 asymmetric stretches were detected around 3015 and 2996 cm^{-1}. However, in the FTIR and Raman spectra (Fig. 5), these peaks were observed at 2966 and 2973 cm^{-1}, respectively. The anticipated asymmetric deformation peak for methyl groups lies between 1465 and 1440 cm^{-1}. Peaks at 1476 and 1492 cm^{-1} in the theoretical spectrum are attributed to the CH_3 group's asymmetric deformation. The CH_3 scissoring mode is represented by peaks at 1423 cm^{-1} in the FTIR and 1436 cm^{-1} in the Raman spectrum, with a corresponding 1447 cm^{-1} peak in the simulated spectrum. This shift can be attributed to the influence of the surrounding molecular environment, possibly including weak hydrogen bonding or van der Waals interactions. Such interactions can slightly alter the electron density around the CH_3 group, leading to a change in bond strength and consequently, a shift in vibrational frequency.

The asymmetric and symmetric CH_2 stretches are typically around 2972 and 2853 cm^{-1}. The FTIR and Raman spectra showed these vibrations at 2926 and 2929 cm^{-1}, respectively. The simulated spectrum displayed the asymmetric CH_2 stretch between 2977 and 2925 cm^{-1}, with the symmetric stretch observed at 2845 cm^{-1} in the Raman spectrum and simulated vibrations at 2920 and 2865 cm^{-1}. The observed shifts in the CH_2 stretching vibrations suggest a subtle change in the electronic environment around these groups, possibly due to intermolecular forces such as hydrogen bonding with nearby functional groups or dipole–dipole interactions within the crystal lattice.

Aromatic amine groups predominantly exhibit C–N stretching absorption between 1335 and 1250 cm^{-1} and 1280–1191 cm^{-1}. This frequency often gets overshadowed due to interference from other bands. FTIR peaks at 1340, 1288, 1209, and 1171 cm^{-1} and Raman peaks at 1322, 1241, and 1220 cm^{-1} in (I) are linked to C–N stretching vibrations. The simulated spectrum identified these vibrations at 1335, 1274, 1255, 1202, and 1191 cm^{-1}. Further, the carboxylate anion in (I) possesses two C = O bonds, with bond strengths between C = O and C–O. The asymmetric and symmetric carboxylate stretches are typically between 1650 and 1549 cm^{-1} and around 1390 cm^{-1}. The FTIR and Raman spectra identified these stretches at 1566 and 1563 cm^{-1}, respectively, with the simulated spectrum showing it at 1595 cm^{-1}. Peaks at 1401 and 1409 cm^{-1} represent symmetric carboxylate stretches, with the simulated spectrum displaying this at 1426 cm^{-1}. The shift in C–N stretching frequencies can be linked to the interaction of the nitrogen atom in the amine group with the surrounding molecular

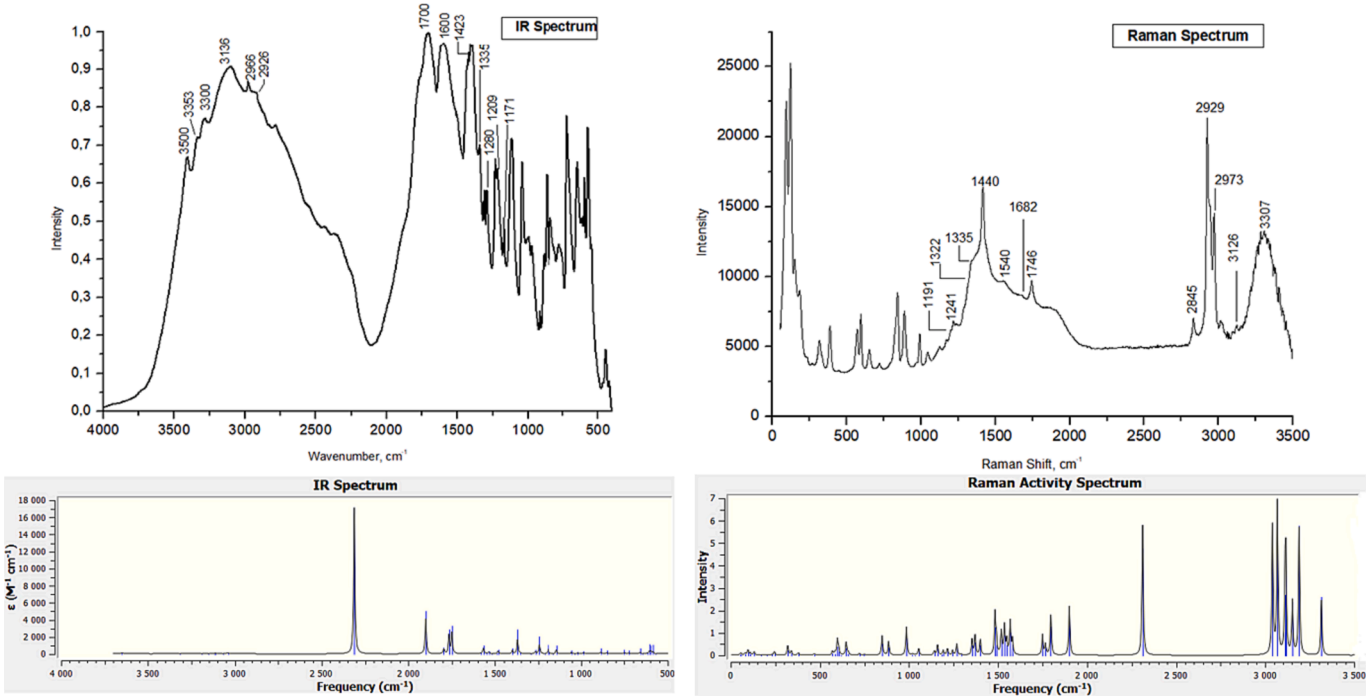

Fig. 5. IR and Raman spectrum of (I).

framework, including potential hydrogen bonding with nearby electronegative atoms. Such interactions can affect the electronic distribution around the nitrogen atom, thereby influencing the C–N bond strength and its vibrational characteristics [48,49].

The comparative analysis of the vibrational modes from both theoretical and experimental spectra has provided a comprehensive understanding of the molecular characteristics of the functional groups under study. Discrepancies between theoretical and experimental vibrational frequencies highlight the role of intermolecular interactions, including hydrogen bonding, in influencing the vibrational behavior of these functional groups in bis(creatininium) succinate. These insights not only add depth to our understanding of the compound's molecular structure but also demonstrate the intricate relationship between molecular interactions and vibrational spectroscopy.

3.3. DFT quantum chemical calculations

Table 3 summarizes the experimental and optimized geometric parameters of (I) using the atom numbering scheme depicted in Fig. 1a. The outcomes obtained revealed a good agreement between the optimized geometric parameters and the structural measurements. Fig. 1b presents the optimized geometry of the most stable arrangement of (I), which exhibits C1 symmetry. It is crucial to highlight that any minor disparities observed between the calculated and observed geometric parameters can be attributed to the inherent dissimilarities in the conditions under which the theoretical computations were conducted, involving isolated molecules in the gaseous phase, compared to the experimental values which are based on molecules within the crystalline state.

In the realm of molecular chemistry and electronic structure, understanding the Highest Occupied Molecular Orbital (HOMO) and the Lowest Unoccupied Molecular Orbital (LUMO) is paramount. These molecular orbitals provide essential insights into a molecule's reactivity, stability, and electronic properties. The energy difference between HOMO and LUMO can be indicative of a molecule's photochemical behaviour and its potential as an electron donor or acceptor.

Furthermore, the Molecular Electrostatic Potential (MEP) offers a visual representation of the molecule's electron distribution. It elucidates regions of electron density and electron scarcity, which is instrumental in predicting sites of reactivity and understanding intermolecular interactions.

Table 3
Selected geometric parameters as determined by X-ray crystallography and theoretical calculations for (I).

(I)	X-Ray	DFT	(I)	X-Ray	DFT
Bond lengths (Å)			**Bond angles (°)**		
Anion			**Anion**		
O2—C6	1.250 (3)	1.243	O1—C6—O2	124.2 (3)	124.9
O1—C6	1.249 (3)	1.254	O1—C6—C7	118.7 (2)	119.1
C6—C7	1.514 (4)	1.521	O2—C6—C7	117.1 (2)	118.3
C7—C7^{i}	1.523 (5)	1.52	C6—C7—C7i	114.50 (19)	115
Cation			**Cation**		
N1—C2	1.357 (3)	1.369	C2—N1—C5	109.8 (2)	110.1
N1—C5	1.369 (4)	1.374	C2—N3—C4	109.5 (2)	109
N3—C2	1.318 (3)	1.325	C2—N3—C3	125.4 (2)	126.4
N3—C4	1.453 (3)	1.46	C4—N3—C3	124.9 (2)	125.8
N3—C3	1.454 (4)	1.459	N2—C2—N3	127.3 (2)	128.8
O5—C5	1.206 (3)	1.217	N2—C2—N1	121.1 (2)	122
C2—N2	1.308 (3)	1.302	N3—C2—N1	111.5 (2)	111.1
C5—C4	1.504 (4)	1.509	O5—C5—N1	125.7 (3)	126
			O5—C5—C4	127.7 (3)	128.1
			N1—C5—C4	106.6 (2)	106.8
			N3—C4—C5	102.5 (2)	103

3.4. Frontier Molecular Orbital (FMO) Analysis

The electronic properties and reactivity of molecules can often be explained by examining their frontier molecular orbitals, namely the Highest Occupied Molecular Orbital (HOMO) and the Lowest Unoccupied Molecular Orbital (LUMO). These orbitals, being the outermost boundaries of a molecule's electronic structure, play pivotal roles in various chemical processes, especially those involving electron transfer. The HOMO is primarily responsible for electron-donating or nucleophilic reactions. A molecule with a relatively high-energy HOMO is typically a good electron donor and can readily participate in processes like oxidation or nucleophilic attacks. Conversely, the LUMO represents the next available or vacant molecular orbital that electrons can occupy. Molecules with low LUMO energies are generally good electron acceptors and can participate in reduction or electrophilic attacks [50,51]. The energy gap between the HOMO and LUMO, often referred to as the HOMO-LUMO gap, is a significant descriptor of molecular reactivity. A smaller HOMO-LUMO gap implies that a molecule can be easily excited, making it more reactive. This gap can be used to predict photochemical behaviour, electronic transitions, and even the colour of certain compounds.

In Fig. 6 the HOMO is localized on the succinate anion, while the LUMO is localized on the creatininium cation. This distinction implies that the succinate anion primarily acts as an electron donor, or a nucleophile, while the creatininium cation can act as an electron acceptor or an electrophile. This spatial separation of the HOMO and LUMO on different parts of the molecule can lead to intramolecular charge transfer, which can significantly affect the molecule's reactivity and properties.

A HOMO-LUMO gap of 2.8864 eV is relatively large, suggesting that the molecule is stable against random electronic excitations. This large gap means that the molecule will likely be resistant to undergoing rapid electron transfer reactions. It also suggests that the compound might

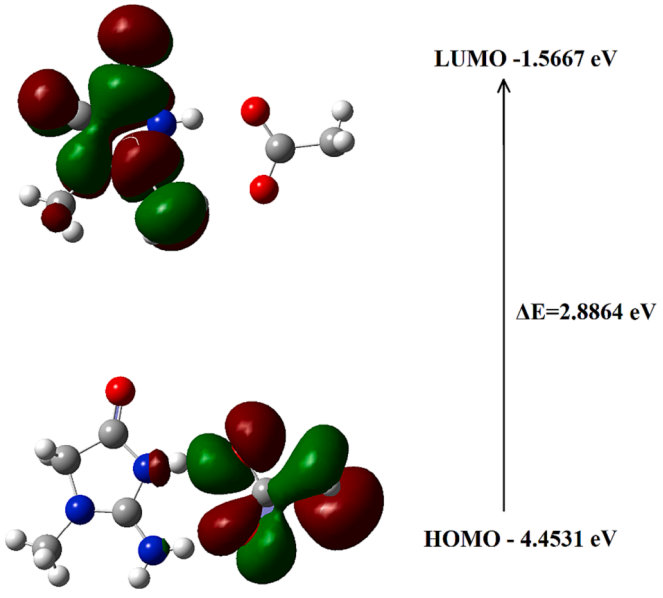

Fig. 6. The frontier molecular orbitals of (I).

exhibit a high photochemical stability, making it less prone to degrade upon exposure to light. Such stability is crucial for potential applications, especially in environments with variable light conditions, ensuring longevity and consistent performance.

The electronic properties of the compound, as deduced from its HOMO and LUMO energy levels, showcase its potential stability and its differential reactivity sites. The distinct localization of the frontier orbitals on the succinate anion and creatininium cation respectively could lead to specific and targeted reactions, making the compound of interest for various applications, especially where selectivity and stability are paramount.

3.5. Molecular Electrostatic Potential (MEP)

The Molecular Electrostatic Potential (MEP) provides a vivid representation of the electron distribution in a molecule, revealing regions of electron density and electron scarcity. By interpreting the MEP, we can predict potential sites of reactivity and understand intermolecular interactions.

In Fig. 7, the presence of a red-yellow region around the succinate moiety indicates areas of high electron density or negative electrostatic potential. This suggests that the succinate part of the molecule is electron-rich and is a region that can act as a nucleophile, i.e., it can donate electrons. Such regions are often attractive to electrophilic species, indicating that electrophiles might preferentially react with the succinate anion.

Conversely, the blue-green region around the creatininium cation signifies areas of low electron density or positive electrostatic potential. This indicates that the creatininium part is electron-deficient and can act as an electrophile, i.e., it can accept electrons. This region is likely to be attractive to nucleophilic species, suggesting that nucleophiles might target the creatininium cation for reactions.

The MEP of (I) (Fig. 7) paints a clear picture of its electronic landscape. The distinct regions of electron density around succinate and electron scarcity around creatininium corroborate with our earlier interpretation from the HOMO and LUMO analysis. Succinate, being electron-rich, is poised to engage in interactions with electrophilic species, while the electron-deficient creatininium is primed for interactions with nucleophiles. This differential electronic character can lead to specific and targeted reactions, offering avenues for tailored chemical modifications and interactions. The MEP, combined with the frontier molecular orbital analysis, provides a comprehensive understanding of the compound's electronic behaviour, guiding chemists in predicting its reactivity and interactions in various scenarios.

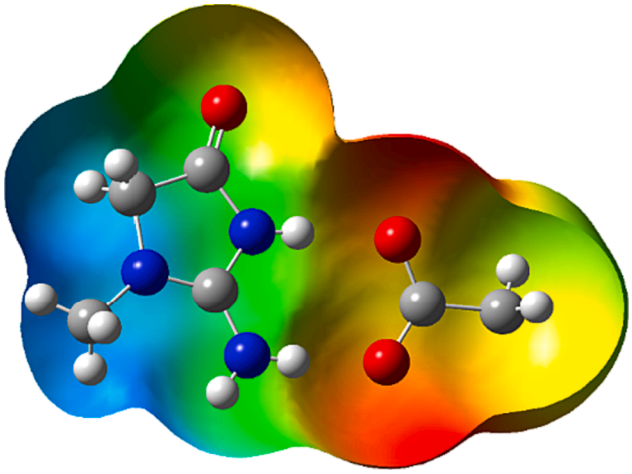

Fig. 7. Molecular electrostatic potential (MEP) surface of (I).

3.6. Hirshfeld surface analyses

Hirshfeld surface analysis is a robust technique employed to visualize and understand intermolecular interactions within crystal structures. This method hinges on the concept of dissecting the electron density of a crystal, and apportioning it into individual molecular fragments. By doing so, it offers profound insights into the nature and potency of the interactions holding the crystal lattice together, making it invaluable for rationalizing a compound's physical and chemical properties. A derivative of this surface analysis is the Hirshfeld fingerprint plot, a graphical portrayal that signifies the fraction of the Hirshfeld surface corresponding to specific normalized contact distances. This fingerprint plot serves as an instrumental tool to not only quantify but also to juxtapose the myriad types of intermolecular interactions prevalent in a crystal structure. In the realm of scientific research, especially in drug design, these methodologies are indispensable. They shed light on the intricate ways in which a drug molecule behaves within its crystalline form or when interacting with its intended target, offering pivotal data that can drive innovative drug development.

In this paper, alongside the conventional X-ray diffraction analysis, we have employed Hirshfeld surface analysis to provide a more nuanced understanding of the intermolecular interactions within the crystal structure of bis(creatininium) succinate. While X-ray diffraction is adept at elucidating the overall molecular geometry and lattice structure, Hirshfeld surface analysis complements these findings by offering detailed insights into the electron density distribution and the nature of specific intermolecular contacts. This analysis is particularly crucial in quantifying the extent of hydrogen bonding and other non-covalent interactions, which are key determinants of the molecular packing and stability in the crystal lattice. The combination of these techniques allows for a comprehensive understanding of both the geometric arrangement and the interaction dynamics within the crystal, enhancing our knowledge of the material's properties and potential applications. Hence, the inclusion of Hirshfeld surface analysis is not merely an adjunct but a necessary expansion to the structural analysis provided by X-ray diffraction, ensuring a more complete and in-depth exploration of the material's characteristics.

The Hirshfeld surfaces of (I) were mapped over d_{norm} and are depicted in Fig. 8A and B. The red circular depressions visible in the front and back surface views indicate hydrogen bonding contacts. The strongest and shortest interactions are due to N–H ··· O hydrogen bonds manifest in the Hirshfeld surfaces as the five (05) red areas. The other visible spots on the surfaces correspond to weak and non-conventional C–H ··· O hydrogen bonds. So, the colour intensity exhibits the intensity of interaction. Further, the electrostatic interaction between creatinium cations becomes evident at the surface within the creatinium ring, primarily due to the interaction involving the lone pair of electrons on the oxygen atom. This phenomenon, elucidated through the utilization of Hirshfeld surface analysis, underscores the distinctive electrostatic characteristics within the creatinium molecular framework.

In (I) structure, O···H/H···O contacts, which are attributed to N—H···O hydrogen-bonding interactions, appear as two sharp symmetric spikes in the two-dimensional fingerprint maps (Fig. 8D). They play a paramount role in shaping the overall Hirshfeld surfaces, and have the most significant contribution to the total Hirshfeld surfaces, with a percentage of 43.1 %. The presence of these long spikes is characteristic of strong hydrogen bonds which exhibit the shortest contacts at *ca* 1.66 Å indicative of the anion-cation interactions.

In the two-dimensional fingerprint maps, the H···H contacts (Fig. 8E) are positioned centrally among the dispersed points. These contacts rank as the second most significant contributors to the Hirshfeld surface, following the O···H/H···O contacts, and they account for 41.5 % of the entire surface. Moreover, the fingerprint plot of (I) displays the presence of the shortest H···H contacts at *ca* 2.38 Å, attributed to N2—H3···H7B—C7 interaction.

Shape index and curvedness (Fig. 9) are geometrical descriptors that

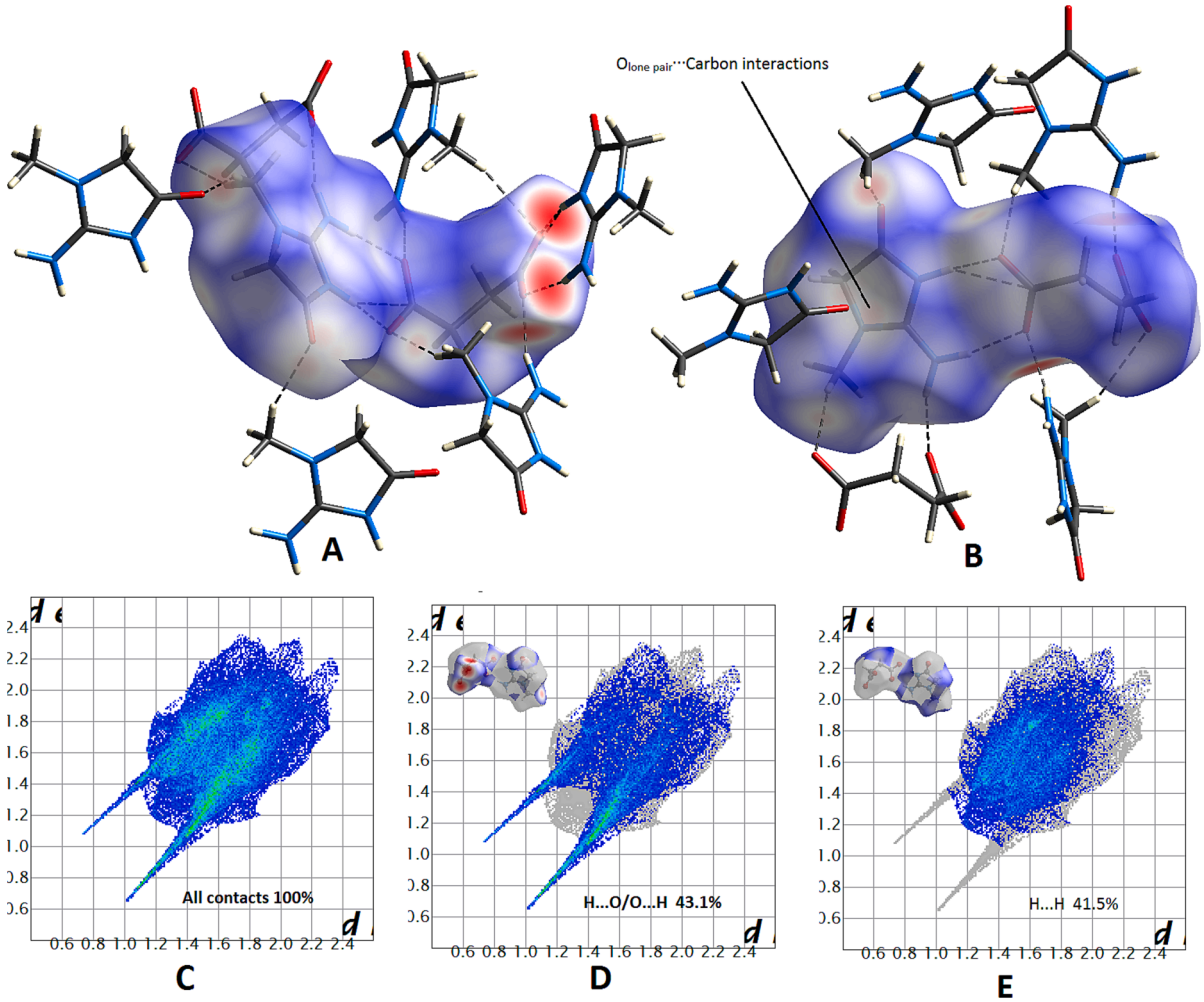

Fig. 8. **A** and **B**: Two different views of HS mapped with d_{norm} of (I) showing the intermolecular interactions. Red circles indicate short and conventional hydrogen bonds. **C, D** and **E** fingerprint plots of (I). (For interpretation of the references to colour in this figure legend, the reader is referred to the web version of this article.)

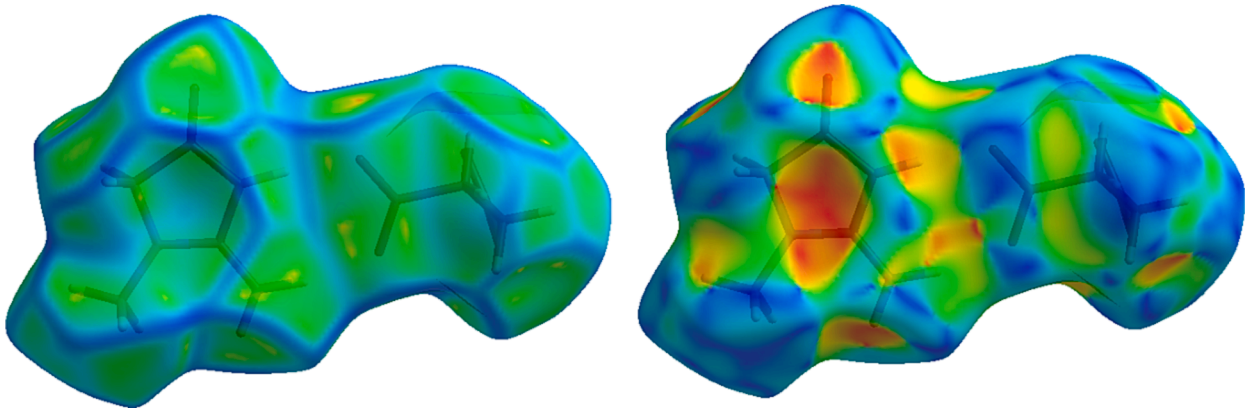

Fig. 9. HS mapped with (left) curvedness and (right) shape index.

offer a nuanced perspective on the morphology of molecular surfaces, particularly the Hirshfeld surface. The shape index, which ranges between −1 and 1, conveys information about the local shape of the surface. Specifically, it can differentiate between shapes like saddles, ridges, valleys, caps, or domes, each associated with a distinct range of values. On the other hand, curvedness provides a measure of the magnitude or intensity of curvature at each point on the surface. In essence, while the shape index categorizes the nature of the surface curvature, curvedness quantifies its degree. By employing these two parameters in tandem, researchers can unravel the intricate topographical features of molecular surfaces, which are often instrumental in dictating intermolecular interactions in crystalline structures. Such an understanding is crucial, as the nuances of these surfaces can profoundly influence molecular behaviour, packing motifs in crystals, and even intermolecular forces that contribute to the stability and properties of crystalline materials.

4. Conclusion

The intricate interplay of molecules within the creatininium-succinate system, as revealed through our multi-faceted study, underscores the profound importance of understanding both structural and electronic nuances. Utilizing X-ray crystallography, we were able to delve deep into the heart of the system, unravelling the key roles played by hydrogen bonds in ensuring the system's stability and cohesion. The hydrogen bonds are fundamental to the crystal lattice's structure, highlighting the system's stability and capacity for specific interactions.

Furthermore, the vibrational spectroscopy analysis has illuminated the vibrational characteristics of the compound's key functional groups. The insights gleaned from both infrared (IR) and Raman spectra have not only validated the structural findings but also enriched our understanding of the compound's molecular dynamics. Discrepancies observed between the theoretical and experimental vibrational modes reinforce the intricate intermolecular interactions and the profound role of hydrogen bonding within the system.

Beyond the structural and vibrational insights, the deep dive into the molecular interactions, especially through the Hirshfeld surface analysis, provides a comprehensive landscape of the compound's interaction dynamics. The presence of both strong N—H···O hydrogen bonds and the more subtle, yet crucial, C—H···O interactions craft a rich tapestry of intermolecular forces that dictate the system's behaviour, packing motifs, and stability.

In summary, the novel contributions of this research can be encapsulated in the comprehensive approach adopted to decipher the creatininium-succinate system. Distinct from existing studies, our research elucidates the coalescence of structural and electronic intricacies through an advanced multi-faceted analysis, which has been underexplored in current literature. The meticulous characterization of hydrogen bonding patterns and vibrational properties, coupled with the innovative use of FMO and MEP analyses, imparts a new perspective on the stabilization mechanisms and reactivity of the system. The intermolecular interactions revealed by Hirshfeld surface analysis further distinguish our work, offering granular insights that could have profound implications for drug design and materials science. Hence, these findings not only augment our scientific comprehension but also highlight potential avenues for exploiting the system's distinct characteristics in areas like molecular engineering and advanced materials research.

CRediT authorship contribution statement

Wahiba Falek: Visualization, Validation, Conceptualization, Project administration, Software. **Radhwane Takouachet:** Investigation, Visualization, Validation, Methodology, Software. **Rim Benali-Cherif:** Methodology, Validation, Conceptualization, Data curation, Funding acquisition, Investigation, Software, Visualization, Writing - original draft, Writing - review & editing. **Sonia Baaziz:** Conceptualization, Validation, Software. **Nourredine Benali-Cherif:** Conceptualization, Investigation, Resources, Software, Supervision, Validation, Visualization.

Declaration of competing interest

The authors declare that they have no known competing financial interests or personal relationships that could have appeared to influence the work reported in this paper.

Data availability

Data will be made available on request.

Acknowledgements

We gratefully acknowledge Professor D. Luneau and Mr. G. Pilet from the University of Claude Bernard Lyon 1 for providing access to the X-ray diffraction platform. We are grateful to Prs A. Djelloul and A. Boumaza for performing the IR measurements.We also thank the Algerian MESRS (Ministère de l'Enseignement Supérieur et de la Recherche Scientifique) and DGRSDT (Direction Générale de la Recherche Scientifique et du Développement Technologique) and Abbes Laghrour Khenchela University, for financial support.

Appendix

The crystallographic data for (I) reported in this work is deposited at the Cambridge Crystallographic Data Center under CCDC N∘. 2288855. These data may be available through the Cambridge Crystallographic Data Centre, 12 Union Road, Cambridge CB2 1EZ, UK; fax: (+44) 1223–336–033; email via. ku.ca.mac.cdcc@tisoped.

Appendix A. Supplementary material

Supplementary data to this article can be found online at https://doi.org/10.1016/j.inoche.2023.111806.

References

[1] J. Wen, L. Li, R. Ping, S. Shang, W. Zhao, M. Hai, H. Cao, X. Yuan, D. Wang, W. He, Z. Yang, Synthesis and Characterization of New Benzo[e]Indol Salts for Second-Order Nonlinear Optics, Crystals 10 (2020) 242.
[2] S. Huang, D.S. Venables, S.E. Lawrence, Pharmaceutical Salts of Piroxicam and Meloxicam with Organic Counterions, Cryst. Growth. Des. 22 (11) (2022) 6504–6520.
[3] X.-N. Hua, X. Pan, Y. Zhu, Z. Cai, Q.i. Song, Y. Li, W. Feng, X. Chen, H. Zhang, B. Sun, Novel pharmaceutical salts of cephalexin with organic counterions: structural analysis and properties, RSC Adv. 12 (54) (2022) 34843–34850.
[4] R. Takouachet, R. Benali-Cherif, N. Benali-Cherif, Cytosinium hydrogen selenite, Acta Cryst. E 70 (2014) o186–o0187.
[5] W. Falek, R. Benali-Cherif, L. Golea, S. Samai, N. Benali-Cherif, E.-E. Bendeif, I. Daoud, A structural comparative study of charge transfer compounds: Synthesis, crystal structure, IR, Raman-spectroscopy, DFT computation and hirshfeld surface analysis, J. Mol. Struct. 1192 (2019) 132–144.
[6] A. Bhar, J.P. Aune, N. Benali-Cherif, L. Benmenni, M. Giorgi, Three Polychloromononitrobenzenes: $C_6H_3Cl_2NO_2$, $C_6H_2Cl_3NO_2$ and $C_6HCl_4NO_2$, Acta Cryst. C 51 (1995) 256–260.
[7] A.S. Kazachenko, Y.N. Malyar, N.Y. Vasilyeva, V.S. Borovkova, N. Issaoui, Optimization of guar gum galactomannan sulfation process with sulfamic acid, Biomass Convers. Biorefin. 13 (11) (2023) 10041–10050.
[8] E. Ulambayar, D. Bor, N.-E. Sukhbaatar, N. Usukhbayar, U. Ganbold, O. Byambasuren, U. Enkhbayar, O. Byambasukh, Handgrip Strength Is Positively Associated with 24-hour Urine Creatine Concentration, Int. J. Environ. Res. Public Health. 20 (2023) 5191.
[9] K. Kalantari, W.K. Bolton, A good reason to measure 24-hour urine creatinine excretion, but not to assess kidney function, Clin. J. Am. Soc. Nephrol. 8 (2013) 1847–1849.
[10] W.E. Magee, R. Burris, Activité oxydative et fixation de l'azote dans les préparations sans cellules d'Azotobacter vinelandii, J. Bacteriol. 71 (1956) 635–643.
[11] P. Chang, H. Hsu, G. Jang, Biological routes to itaconic and succinic acids, Pure and Applied, Chemistry 88 (2016) 799–810.
[12] R. Takouachet, R. Benali-Cherif, E.-E. Bendeif, C. Jelsch, F. Yahia Cherif, A. Rahmouni, N. Benali-Cherif, The supramolecular behavior and molecular recognition of adeninium cations on anionic hydrogen selenite/diselenite frameworks: A structural and theoretical analysis, J. Mol. Struct. 1229 (2021).
[13] H. Athmani, C. Kijatkin, R. Benali-Cherif, S. Pillet, D. Schaniel, M. Imlau, N. Benali-Cherif, E.-E. Bendeif, Nonlinear optical organic–inorganic crystals: synthesis, structural analysis and verification of harmonic generation in tri-(o-chloro-anilinium nitrate), Acta Cryst. A 75 (2019) 107–114.
[14] A.S. Kazachenko, N. Issaoui, A. Sagaama, Y.N. Malyar, O. Al-Dossary, L. G. Bousiakou, A.S. Kazachenko, A.V. Miroshnokova, Z. Xiang, Hydrogen bonds interactions in biuret-water clusters: FTIR, X-ray diffraction, AIM, DFT, RDG, ELF, NLO analysis, Journal of King Saud University - Science 34 (8) (2022) 102350.
[15] A. Jumabaev, U. Holikulov, H. Hushvaktov, N. Issaoui, A. Absanov, Intermolecular interactions in ethanol solution of OABA: Raman, FTIR, DFT, M062X, MEP, NBO, FMO, AIM, NCI, RDG analysis, J. Mol. Liq. 377 (2023) 121552.
[16] C.R. Groom, I.J. Bruno, M.P. Lightfoot, S.C. Ward, The Cambridge Structural Database, Acta Cryst. B 72 (2016) 171–179.
[17] R. Benali-Cherif, R. Takouachet, W. Falek, N. Benali-Cherif, C. Jelsch, H. Merazig, M. Hafied, E.-E. Bendeif, N. Bouslah Mokhnachi, K. Taibi, Synthesis, structural

elucidation, spectroscopic, Hirshfeld surface analysis and theoretical simulation of a new adeninium orthoperiodate (1−) bis(hydrate) organic–inorganic hybrid crystals, Molecular Structure. 1224 (2021), 129034.
[18] I. Sivagami, RO.MU. Jauhar, P. Era, V. Viswanathan, G. Vinitha, S. Ranjani, T. Sivanesan, Growth, structural, spectral, Hirshfeld analysis, photoluminescence, linear and third order NLO properties of a novel organic p-toluidinium succinate succinic acid single crystal, J. Cryst. Growth. 580 (2022) 126471.
[19] S. Rekha Rout, G. Kenguva, L. Giri, R. Dandela, Novel salts of the antiemetic drug domperidone: synthesis, characterization and physicochemical property investigation, CrstEngComm 25 (4) (2023) 513–524.
[20] J. Li, D.i. Wu, Y. Xiao, C. Li, X.u. Ji, Q. Sun, D. Chang, L. Zhou, D. Jing, J. Gong, W. Chen, Salts of 2-hydroxybenzylamine with improvements on solubility and stability: Virtual and experimental screening, Eur. J. Pharm. Sci. 169 (2022) 106091.
[21] S. Sindhusha, C.M. Padma, B. Gunasekaran, Crystal structure, spectroscopic characterization, mechanical, thermal and theoretical investigations on creatininium benzenesulfonate - A new organic NLO single crystal, J. Mol. Struct. 1221 (2020) 128863.
[22] S. Surya, B. Gunasekaran, T.C.S. Girisun, Synthesis, growth, crystal structure, thermal, optical, electrical and third-order nonlinear optical properties of creatininium phthalate as a new nonlinear optical single crystal, J Mater Sci: Mater Electron. 33 (2022) 8683–8701.
[23] O. Noureddine, N. Issaoui, S. Gatfaoui, O. Al-Dossary, H. Marouani, Quantum chemical calculations, spectroscopic properties and molecular docking studies of a novel piperazine derivative, Journal of King Saud University –, Science 33 (2) (2021) 101283.
[24] R. Takouachet, R. Benali-Cherif, E.-E. Bendeif, N. Benali-Cherif, S. Pillet, D. Schaniel, Structural analysis and IR-spectroscopy of a new anilinium hydrogenselenite hybrid compound: A subtle structural phase transition, Inorg. Chim. Acta 446 (2016) 6–12.
[25] M.C. Burla, R. Caliandro, B. Carrozzini, G.L. Cascarano, C. Cuocci, C. Giacovazzo, M. Mallamo, A. Mazzone, G. Polidori, Crystal structure determination and refinement via SIR2014, J. Appl. Cryst. 48 (2015) 306–309.
[26] G.M. Sheldrick, Crystal structure refinement with SHELXL, Acta Cryst. C 71 (2015) 3–8.
[27] L.J. Farrugia, WinGX and ORTEP for Windows: an update, J. Appl. Crystallogr. 45 (4) (2012) 849–854.
[28] C.F. Macrae, I. Sovago, S.J. Cottrell, P.T.A. Galek, P. McCabe, E. Pidcock, M. Platings, G.P. Shields, J.S. Stevens, M. Towler, P.A. Wood, Mercury 4.0: from visualization to analysis, design and prediction, J. Appl. Cryst. 53 (2020) 226–235.
[29] J. de Meulenaer, H. Tompa, The absorption correction in crystal structure analysis, Acta Cryst 19 (6) (1965) 1014–1018.
[30] A.D. Becke, Density-functional thermochemistry. III. The role of exact exchange, J. Chem. Phys. 98 (1993) 5648–5652.
[31] D. Jacquemin, J. Preat, M. Charlot, V. Wathelet, J.-M. André, E.A. Perpète, Theoretical investigation of substituted anthraquinone dyes, J. Chem. Phys. 121 (2004) 1736–1743.
[32] T.J. Ajayi, M. Shapi, Solvent-free mechanochemical synthesis, hirshfeld surface analysis, crystal structure, spectroscopic characterization and NBO analysis of Bis (ammonium) Bis ((4-methoxyphenyl) phosphonodithioato)-nickel (II) dehydrate with DFT studies, J. Mol. Struct. 1202 (2020), 127254.
[33] S. Brahim, H. Brahim, S. Humbel, A. Rahmouni, Computational studies of Ni (II) photosensitizers complexes containing 1, 1′-bis (diphenylphosphino) ferrocene and dithio ligands, Can. J. Chem. 98 (4) (2020) 194–203.
[34] M.J. Frisch, G.W. Trucks, H.B. Schlegel, G.E. Scuseria, M.A. Robb, J.R. Cheeseman, G. Scalmani, V. Barone, B. Mennucci, G.A. Petersson, H. Nakatsuji, M. Caricato, X. Li, H.P. Hratchian, A.F. Izmaylov, J. Bloino, G. Zheng, J.L. Sonnenberg, M. Hada, M. Ehara, K. Toyota, R. Fukuda, J. Hasegawa, M. Ishida, T. Nakajima, Y. Honda, O. Kitao, H. Nakai, T. Vreven, J.A. Montgomery, Jr., J.E. Peralta, F. Ogliaro, M. Bearpark, J.J. Heyd, E. Brothers, K.N. Kudin, V.N. Staroverov, R. Kobayashi, J. Normand, K. Raghavachari, A. Rendell, J.C. Burant, S.S. Iyengar, J. Tomasi, M. Cossi, N. Rega, J.M. Millam, M. Klene, J.E. Knox, J.B. Cross, V. Bakken, C. Adamo, J. Jaramillo, R. Gomperts, R.E. Stratmann, O. Yazyev, A.J. Austin, R. Cammi, C. Pomelli, J.W. Ochterski, R.L. Martin, K. Morokuma, V.G. Zakrzewski, G.A. Voth, P. Salvador, J.J. Dannenberg, S. Dapprich, A.D. Daniels, Ö. Farkas, J.B. Foresman, J. V. Ortiz, J. Cioslowski, and D.J. Fox, Gaussian 09, Revision A.02, Gaussian, Inc., Wallingford CT, 2009.
[35] R.D. Dennington, T.A. Keith, J.M. Millam, Structural and Spectral (IR, NMR and UV/Visible) Properties of Newly Designed Boronic Acid Derivatives Containing DO3A Sensitive to Uranyl Ion: A DFT and TD-DFT Study, GaussView 5.0.8, Gaussian Inc., Wallingford, CT, 2008.
[36] N.M. O'boyle, A.L. Tenderholt, K.M. Langner, Software News and Updates cclib: A Library for Package-Independent Computational Chemistry Algorithms, J. Comp. Chem. 29 (5) (2008) 839–845.
[37] M.A. Spackman, J.J. McKinnon, Fingerprinting intermolecular interactions in molecular crystals, CrstEngComm 4 (66) (2002) 378–392.
[38] M.A. Spackman, P.G. Byrom, A novel definition of a molecule in a crystal, Chem. Phys. Lett. 267 (3-4) (1997) 215–220.
[39] J.J. McKinnon, M.A. Spackman, A.S. Mitchell, Novel tools for visualizing and exploring intermolecular interactions in molecular crystals, Acta Crystallogr. B 60 (6) (2004) 627–668.
[40] S.K. Wolff, D.J. Grimwood, J.J. McKinnon, M.J. Turner, D. Jayatilaka, M.A. Spackman, CrystalExplorer, Version 3.1, University of Western Australia, Perth, 2012.
[41] L. A. Deschenes, A. David, A. Vanden, Origin 6.0: Scientific Data Analysis and Graphing Software Origin Lab Corporation (formerly Microcal Software, Inc.). Web site: www.originlab.com. Commercial price: $595. Academic price: $446, Computer Software ReViews. J. Am. Chem. Soc.122 (2000), 39, 9567–9568.
[42] S. Sindhusha, C.M. Padma, B. Gunasekaran, Creatininium phosphite, IUCrData. 2 (2017), x171043.
[43] N. Jeyaraman Selvaraj, U. Sathya, S. Gomathi, S. Jegan Jennifer, L. Mathivathanan, I. Abdul Razak, Synthesis, crystal structure determination and Hirshfeld surface analysis of three new salt forms of creatinine with hydro-bromic acid, 3-amino-benzoic acid and 3,5-di-nitro-benzoic acid, Acta Crystallographica Section C: Structural Chemistry, C 78 (8) (2022) 437–448.
[44] S. Sindhusha,a C. M. Padmab and B. Gunasekaran, IUCrData. 2 (2017), x171043.
[45] A.S. Kazachenko, M. Medimagh, N. Issaoui, O. Al-Dossary, M.J. Wojcik, A. S. Kazachenko, A.V. Miroshnokova, Y.N. Malyar, Sulfamic acid/water complexes (SAA-$H_2O_{(1-8)}$) intermolecular hydrogen bond interactions: FTIR, X-ray, DFT and AIM analysis, J. Mol. Struct. 1265 (2022), 133394.
[46] M. Medimagh, N. Issaoui, S. Gatfaoui, O. Al-Dossary, A.S. Kazachenko, H. Marouani, M.J. Wojcik, Molecular modeling and biological activity analysis of new organicinorganic hybrid: 2-(3,4-dihydroxyphenyl) ethanaminium nitrate, J. King Saud Univ. Sci. 33 (8) (2021) 101616.
[47] C. Moreno Castro, M.C. Ruiz Delgado, V. Hernandez, S. Hotta, J. Casadoc, J. T. Lopez Navarrete, Efficiency of the π conjugation in a novel family of α, α′-bisphenyl end-capped oligothiophenes by means of Raman spectroscopy, J. Chem. Phys. 116 (2002) 10419.
[48] S. Gatfaoui, N. Issaoui, T. Roisnel, H. Marouani, Synthesis, experimental and computational study of a non-centrosymmetric material 3-methylbenzylammonium trioxonitrate, J. Mol. Struct. 1225 (2021), 129132.
[49] N. Rekik, N. Issaoui, B. Oujia, M.J. Wójcik, Theoretical IR spectral density of H-bond in liquid phase: Combined effects of anharmonicities, Fermi resonances, direct and indirect relaxations, J. Mol. Liq. 141 (3) (2008) 104–109.
[50] A.F. Jalbout, B. Trzaskowski, A.J. Hameed, Theoretical investigation of the electronic structure of 1-(3,4; 3,5 and 3,6-bis-selenocyanato-phenyl) pyrrolidinofullerenes, J. Organomet. Chem. 691 (22) (2006) 4589–4594.
[51] A.F. Jalbout, A.J. Hameed, B. Trzaskowski, Study of the structural and electronic properties of 1-(4, 5 and 6-selenenyl derivatives-3-formyl-phenyl) pyrrolidinofullerenes, J. Organomet. Chem. 692 (5) (2007) 1039–1047.